Analysis of RHESSI Flares Using Radio Astronomical Techniques

E.J. Schmahl[1,2], R.L. Pernak[2,3], G.J. Hurford[4]

[1]*Astronomy Department, University of Maryland, College Park, MD 20742*
[2]*Laboratory for Solar and Space Physics, NASA Goddard Space Flight Center, Greenbelt, MD 20771*
[3]*Institute for Astrophysics and Computational Sciences, The Catholic University of America, Washington, DC 20064*
[4]*Space Sciences Laboratory, University of California, Berkeley, CA 94720*

ABSTRACT

We have used Ramaty High Energy Solar Spectroscopic Imager (RHESSI) modulation profiles in the 25-300 keV range to construct high-fidelity visibilities of 25 flares having at least two components. These hard X-ray (HXR) visibilities, which are strictly analogous to the visibilities of radio imaging, were input to software developed for mapping solar flares in the microwave domain using the Maximum Entropy Method (MEM). We compared and contrasted the MEM maps with Clean and Pixon maps made with RHESSI software. In particular, we assessed the reliability of the maps and their morphologies for investigation of the symmetry of bipolar electron beaming in the sample set.

1. Introduction

The Ramaty High Energy Solar Spectroscopic Imager (RHESSI) has been observing flares since February 2002 (Lin et al, 2002). RHESSI is the first HXR imager to use Fourier-based methods with high spectral (~ 1 keV) energy resolution in the 3 keV - 17 MeV range, although previous lower-resolution Fourier-based imagers — Hinotori and Yohkoh/HXT — have provided abundant proof of principle of this method of imaging. The amplitudes and phases of RHESSI's modulation profiles are analogous to the amplitudes and phases derived from radio interferometers (Hurford et al, 2002). After calibration, these amplitudes and phases become device-independent (Hurford et al, 2005), and are precisely equivalent to radio visibilities.

Mapping with visibilities has a rich history in radio astronomy. Visibilities themselves are samples of the Fourier transform of the flare source in the image plane. Given dense sampling of the u,v plane (u and v are the coordinates of the Fourier plane), the inverse

Fourier transform yields a map. Since the u,v sampling is not usually dense, and often quite sparse, the map so produced is called the "dirty map." Various methods have been devised to remove the sidelobes produced by sparse sampling in the dirty map and we selected the Maximum Entropy Method (MEM) for this study.

Other methods of HXR imaging have been developed for RHESSI (Schwartz et al, 2002). Among them are Back-projection, Clean, and Pixons, and these can provide validation and testing of the MEM images.

1.1. RHESSI Visibilities

Each amplitude (A_j) and phase (ϕ_j) computed from RHESSI modulation profiles are combined into visibilities (V_j) in the standard way:

$$V_j = A_j \exp(i\phi) \tag{1}$$

Since RHESSI is a rotation-modulation collimator (RMC) with 9 subcollimators, the (u_j, v_j) samples lie on 9 circles in the Fourier plane (Fig. 1). Each circle has a radius $k_j = \sqrt{u_j^2 + v_j^2}$ given by the reciprocal of the angular pitch of the j^{th} subcollimator (Hurford et al, 2002).

$$k_j = 1/(4.5 * 3^{(j-1)/2}) \text{ arcsec}^{-1}, j = 1, 2, ..., 9 \tag{2}$$

The smallest k_j, for the coarsest subcollimator 9, provides an amplitude closest to the total flux, and the largest k_j, for the finest collimator 1, can in principle provide information on spatial scales of $\sim 2.3''$. For the best (u,v) coverage, one must use as many of the (u,v) circles as possible, consistent with the minimization of "over-resolution" and avoidance of RHESSI's spin axis. Typically, this means using circles 3-8, although some compact flares permit the use of circles 2-8, and some extended sources require restricting the range to 4-8.

1.2. The Maximum Entropy Method

MEM imaging has been widely used in a variety of fields and was first developed by Jaynes (1957, 1968). The basis of the method is to maximize the information entropy H while minimizing a measure of the goodness-of-fit (usually χ^2) and maintaining the correct value of the flux. In practice, following Cornwell and Evans 1985, one maximizes the objective function:

$$J = H - \alpha\chi^2 - \beta F \tag{3}$$

over the parameter space of all possible images. Here, α and β are Lagrange multipliers, χ^2 is the statistical measure of goodness-of-fit to the data, and F is the flux, i.e. the sum of pixel brightnesses. Differentiating equation (3) with respect to pixel brightnesses and setting that gradient equal to zero gives:

$$\nabla J = \nabla H - \alpha \nabla \chi^2 - \beta = 0 \tag{4}$$

Bong et al (2004a, b) have developed a MEM program following these principles which maps Owens Valley Solar Array (OVSA) data. In its original form, it is a 3-D MEM, using not only u,v but frequency ν as a third independent coordinate. The solar group at New Jersey Institute of Technology (NJIT) has provided the 2-D MEM version to the RHESSI team and dubbed it MEM NJIT. We have computed visibilities and input them into the MEM NJIT program, as described below.

2. Observations

We have selected 25 well-resolved double-component flares from the more than 17,000 in the RHESSI dataset. We have a two-fold goal: validate the MEM imaging and provide preliminary statistics on the asymmetry of double-component flares. To accomplish the first goal, we compare MEM with other imaging methods (Clean and Pixons). To address the second goal we measure flux ratios of the component sources and footpoint separations in 25 flares.

Figure 1 shows maps of 25 RHESSI flares made using MEM NJIT. The selection of these flares was not intended to be completely unbiased. As a guide to flare selection, we used the RHESSI flare catalog, taking only flares with $> 10^4$ counts in bands greater than 25 keV. Then we selected a subset where Clean images showed two unambiguous, resolved sources. For the purposes of this paper, we have neglected cases where the double sources overlap, or where one is limb-occulted, or where one source is very weak (the latter case, while interesting, is beyond the scope of this study). We chose the highest energy band (25-50, 50-100, or 100-300 keV) with good statistics and, if possible, no tertiary sources.

Figure 2 shows maps of the same 25 flares made using the RHESSI Clean algorithm with the same number of contour levels as in Fig. 1. There are differences between the Clean maps and the MEM maps, most notably in the apparent "noise" in the lowest (10%) contour. The sources appear to be broader, mainly because the Clean components are convolved with the RHESSI point spread function at the final stage of processing, but also because Clean appears to be more inclusive in tertiary components that MEM does not show (e.g. flares #1 and 21). Comparison of component sizes clearly shows the "super resolution"

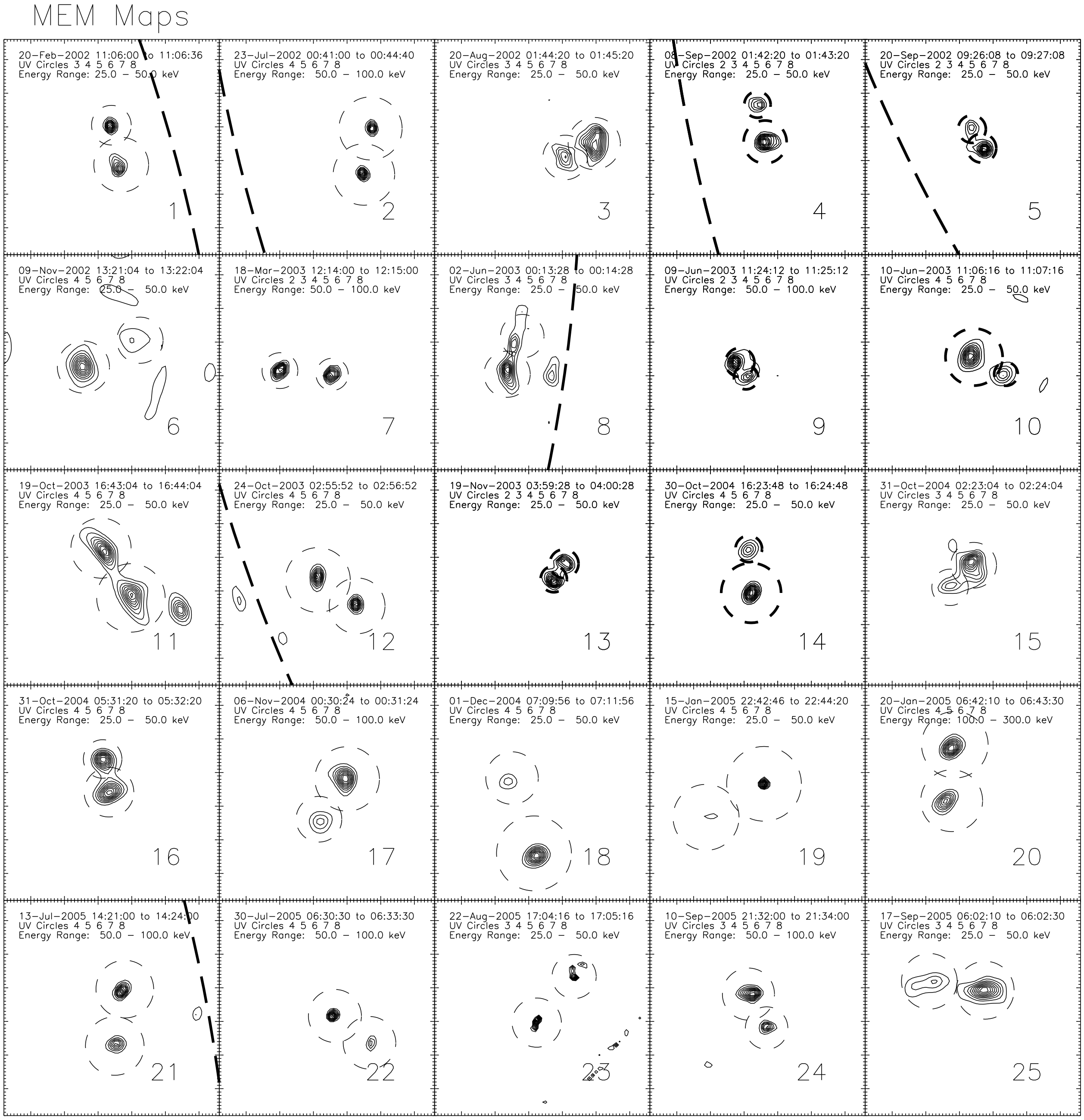

Fig. 1.— MEM NJIT maps of 25 double-component flares in the 25-50 keV band. Contour levels are 10, 20, 30, 40, 50, 60, 70, 80, 90, and 100% of the maximum flux. The spatial scale is 2 arcsec/pixel and the field of view is 128×128 arcsec. The dashed circles represent regions where fluxes were calculated.

that MEM algorithms are known for (Cornwell and Evans 1985). We return to the issue of super-resolution in section 3.4.

Figure 3 is an array of maps for the same 25 flares, this time using the RHESSI Pixon algorithm. Comparison with Fig. 1 shows that the Pixon components, with few exceptions (flares #2 and 22), are similar in size to the MEM components. If the instrumentally-convolved components of the Clean maps are a proper guide, then the Pixon maps seem to show as much "super resolution" as the MEM maps.

To estimate the reliability of MEM maps relative to Clean and Pixons, we have quantified the positions and vectorial separations of the components in all maps. We have computed the centroids (x_1, y_1) and (x_2, y_2) of the MEM NJIT subsources. Using them we computed their de-projected separation (s) measured in Mm at the chromospheric level, and de-projected orientation (α) in radians relative to the local line of latitude. These are tabulated in Table I below.

The first column gives the flare date and time interval; the second and third columns give $centroid_1$ and $centroid_2$, the heliographic centroids (arcsec) of the brighter and weaker sub-sources, respectively; the fourth column gives s, their de-projected separation (Mm); the fifth column gives α, the de-projected orientation (in radians from the local latitude line); in the sixth and seventh columns, $Flux1$ and $Flux2$ are the fluxes of the stronger and weaker components, respectively; the eighth column gives their flux asymmetry ratio, $\frac{Flux_1}{Flux_1+Flux_2}$, as defined by Aschwanden et al (1999).

We have done the same calculations for the Clean and Pixon maps, and the results are shown in Tables II and III.

3. Discussion

Inspection of Figures 1-3 show that the MEM NJIT, Clean, and Pixon images are similar in many respects. To quantify the similarities, we have plotted fluxes, centroids, and histograms of the MEM, Clean, and Pixon parameters.

3.1. Component Fluxes

To assess the reliability of flux measurements, we plot Clean flux as a function of MEM NJIT flux for both components in Figure 4a, Pixon flux as a function of MEM NJIT flux in Figure 4b, and Clean flux as a function of Pixon flux in Figure 4c. All three figures show

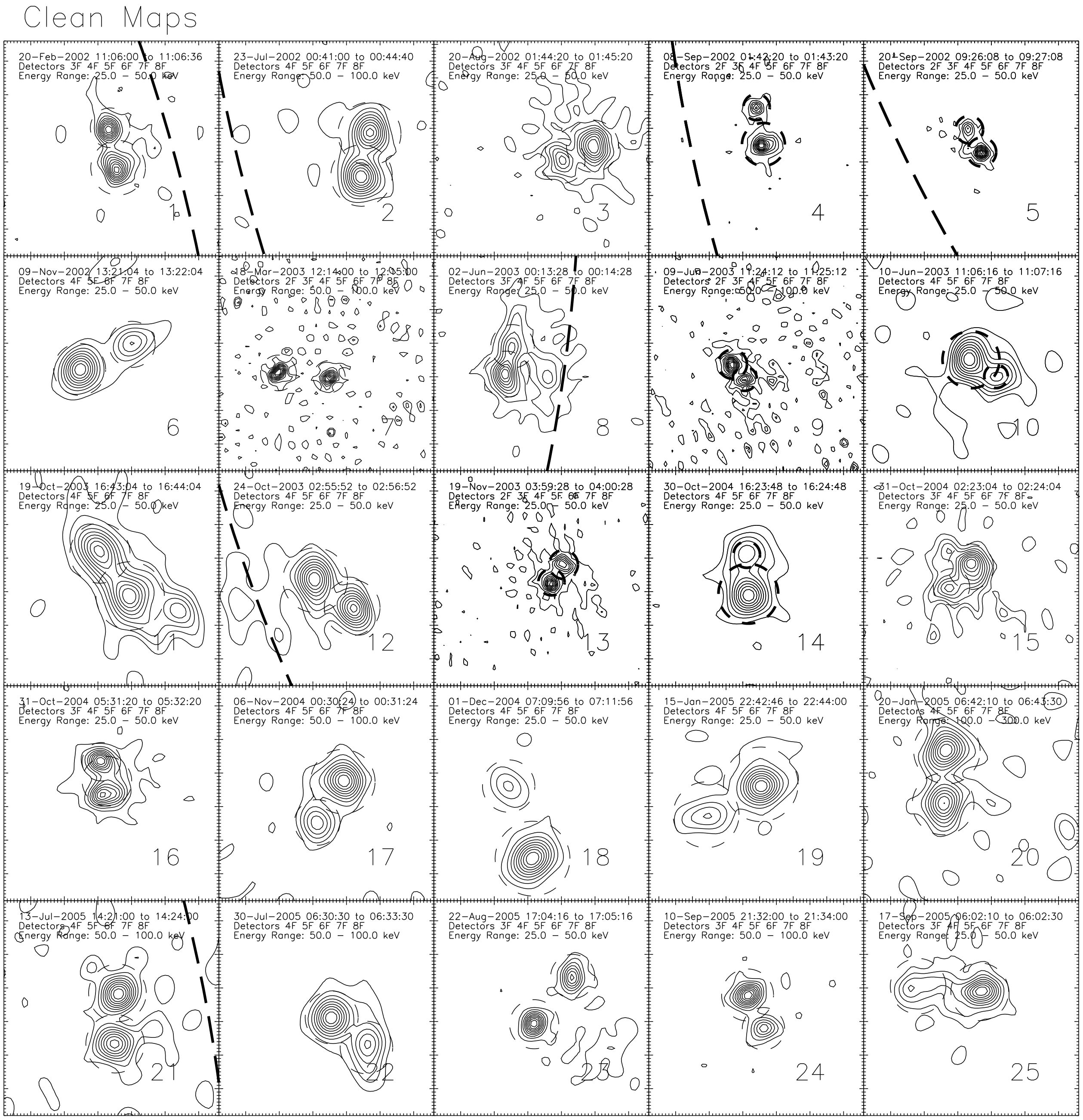

Fig. 2.— Clean maps of the same flares as Fig. 1. The spatial scale is the same (2 arcsec per pixel) and detectors used correspond to the (u,v) circles used in MEM NJIT. Contour levels start at 10% and increase to 100% of the maximum flux by increments of 10%, and the field of view is 128×128 arcsec.

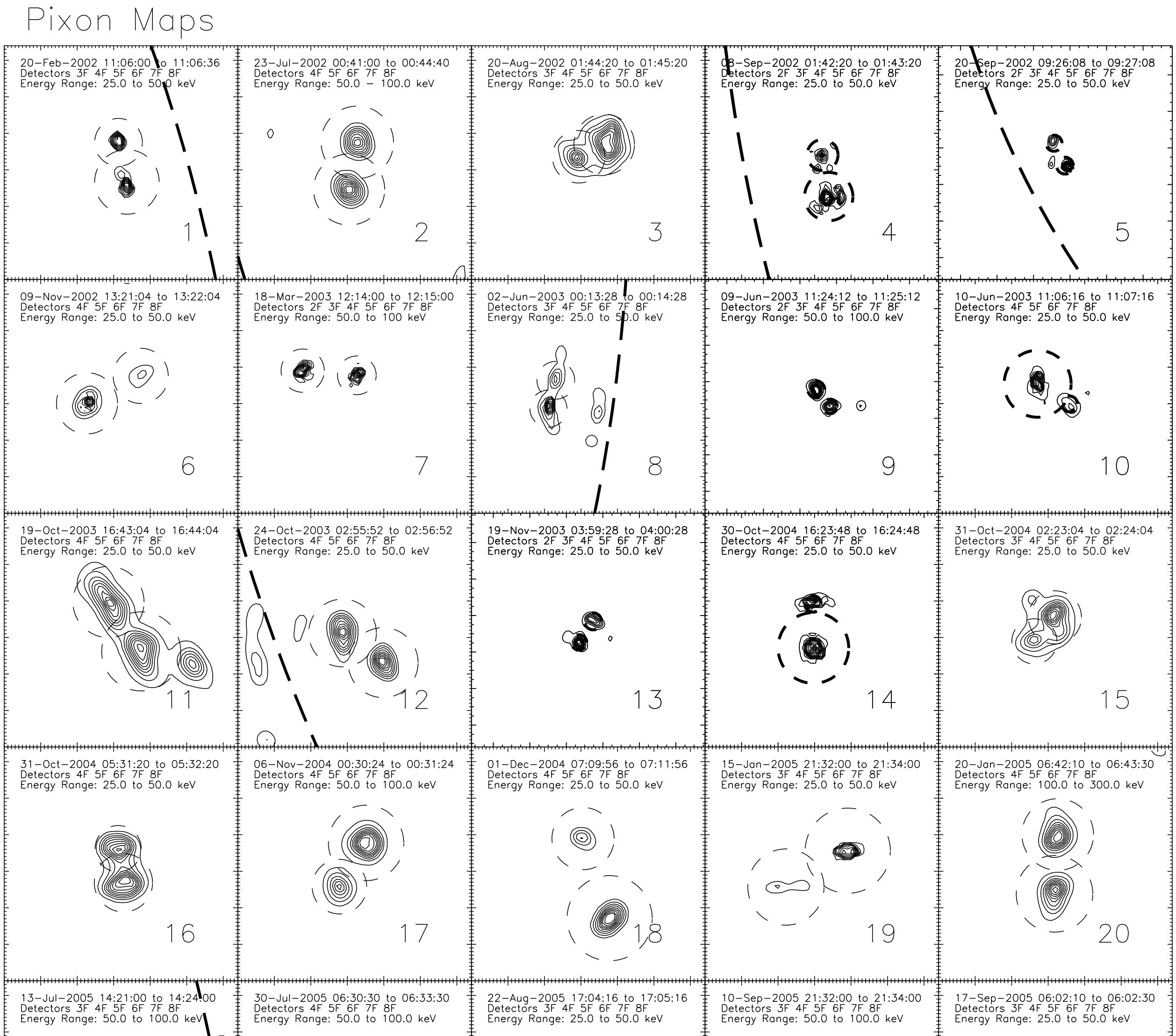

Fig. 3.— Pixon maps of the same flares as Figs. 1 and 2. Again, we use 2 arcsec per pixel, 10%-100% contour levels, and a 128×128 field of view.

TABLE I

MEM NJIT flare statistics

$Date/Time$	$centroid_1$	$centroid_2$	s	α	$Flux1$	$Flux2$	$\frac{Flux1}{Flux1+Flux2}$
2002/02/20 11:06:00-11:06:36	908.0, 248.0	902.0, 272.0	17.67	1.52	23.98	19.48	0.55
2002/07/23 00:41:00-00:44:40	-873.0,-244.0	-871.0,-216.0	32.54	0.88	3.48	3.25	0.52
2002/08/20 01:44:20-01:45:20	540.0,-268.0	522.0,-278.0	15.70	0.41	6.40	2.28	0.74
2002/09/08 01:42:20-01:43:20	-912.0,-199.0	-918.0,-177.0	16.66	1.09	32.83	10.97	0.75
2002/09/20 09:26:08-09:27:08	-834.0,-424.0	-840.0,-412.0	9.32	1.33	22.51	9.67	0.70
2002/11/09 13:21:04-13:22:04	420.0,-267.0	454.0,-251.0	28.35	0.40	37.84	14.45	0.72
2003/03/18 12:14:00-12:15:00	668.0,-160.0	698.0,-162.0	32.63	0.04	7.98	6.70	0.54
2003/06/02 00:13:28-00:14:28	931.0,-137.0	941.0,-115.0	20.00	0.23	19.92	11.06	0.64
2003/06/09 11:24:12-11:25:12	471.0, 227.0	475.0, 219.0	7.04	1.17	12.19	5.39	0.69
2003/06/10 11:06:16-11:07:16	651.0, 229.0	669.0, 219.0	19.84	0.42	9.84	3.18	0.76
2003/10/19 16:43:04-16:44:04	-798.0, 44.0	-816.0, 74.0	33.52	0.61	21.32	17.27	0.55
2003/10/24 02:48:26-02:50:52	-879.0,-330.0	-857.0,-346.0	47.40	0.19	16.33	12.24	0.57
2003/11/19 03:59:28-04:00:28	-96.0, -20.0	-90.0, -10.0	7.94	1.03	19.14	17.83	0.52
2004/10/30 16:23:48-16:24:48	430.0, 128.0	428.0, 154.0	19.09	1.55	80.74	41.81	0.66
2004/10/31 02:23:04-02:24:04	532.0, 161.0	518.0, 149.0	16.27	0.55	5.51	1.73	0.76
2004/10/31 05:31:20-05:32:20	544.0, 142.0	540.0, 162.0	14.53	1.48	17.77	12.40	0.59
2004/11/06 00:30:24-00:31:24	-72.0, 96.0	-90.0, 72.0	21.06	0.94	7.11	2.81	0.72
2004/12/01 07:09:56-07:11:56	-333.0, 107.0	-345.0, 153.0	34.40	1.25	7.07	1.89	0.79
2005/01/15 22:42:46-22:44:00	128.0, 312.0	94.0, 292.0	29.46	0.55	43.61	21.10	0.67
2005/01/20 06:42:10-06:43:30	821.0, 273.0	819.0, 239.0	28.62	1.12	7.53	5.98	0.56
2005/07/13 14:21:00-14:24:00	909.0, 185.0	903.0, 151.0	49.92	0.49	1.70	1.47	0.54
2005/07/30 06:30:30-06:33:30	-812.0, 132.0	-792.0, 116.0	34.05	0.28	20.77	11.00	0.65
2005/08/22 17:04:16-17:05:16	790.0,-253.0	812.0,-225.0	31.94	0.63	27.24	25.90	0.51
2005/09/10 21:32:00-21:34:00	-666.0,-248.0	-656.0,-268.0	16.92	1.09	10.04	4.03	0.71
2005/09/17 06:02:10-06:02:30	638.0,-270.0	606.0,-266.0	34.35	0.18	415.12	198.50	0.68

TABLE II

Clean flare statistics

Date/Time	$centroid_1$	$centroid_2$	s	α	$Flux1$	$Flux2$	$\frac{Flux1}{Flux1+Flux2}$
2002/02/20 11:06:00-11:06:36	908.02, 248.49	903.26, 272.34	18.49	1.43	25.12	18.53	0.58
2002/07/23 00:41:00-00:44:40	-874.02,-242.16	-869.30,-217.27	31.94	0.72	2.50	2.39	0.51
2002/08/20 01:44:20-01:45:20	540.52,-268.58	522.78,-277.41	16.18	0.36	6.98	3.75	0.65
2002/09/08 01:42:20-01:43:20	-911.74,-198.56	-915.79,-176.34	16.68	1.51	34.00	12.46	0.73
2002/09/20 09:26:08-09:27:08	-831.76,-424.13	-839.15,-410.82	11.37	1.13	19.00	11.80	0.62
2002/11/09 13:21:04-13:22:04	419.12,-266.61	450.33,-251.68	26.30	0.41	25.36	9.29	0.73
2003/03/18 12:14:00-12:15:00	667.50,-159.68	697.64,-161.94	31.67	0.04	8.56	7.26	0.54
2003/06/02 00:13:28-00:14:28	932.02,-135.43	935.84,-118.85	18.08	0.76	12.64	7.98	0.61
2003/06/09 11:24:12-11:25:12	468.85, 228.48	476.12, 219.83	8.45	0.89	14.16	9.31	0.60
2003/06/10 11:06:16-11:07:16	650.86, 229.17	665.78, 219.27	15.86	0.50	6.49	2.72	0.70
2003/10/19 16:43:04-16:44:04	-796.82, 47.50	-814.78, 72.96	31.63	0.54	11.45	11.14	0.51
2003/10/24 02:48:26-02:50:52	-879.66,-329.12	-857.61,-345.51	44.60	0.19	11.78	10.24	0.53
2003/11/19 03:59:28-04:00:28	-95.95, -20.36	-88.75, -9.85	9.16	0.97	16.95	16.03	0.51
2004/10/30 16:23:48-16:24:48	429.27, 128.80	428.33, 152.12	17.01	1.51	58.65	25.79	0.69
2004/10/31 02:23:04-02:24:04	531.71, 161.85	520.26, 149.85	13.94	0.64	3.03	1.22	0.71
2004/10/31 05:31:20-05:32:20	543.38, 149.09	540.02, 160.73	8.74	1.38	12.53	8.15	0.61
2004/11/06 00:30:24-00:31:24	-74.17, 94.89	-89.42, 70.55	20.68	1.02	4.32	1.75	0.71
2004/12/01 07:09:56-07:11:56	-332.21, 106.03	-346.42, 149.24	33.59	1.19	5.94	1.16	0.84
2005/01/15 22:42:46-22:44:00	128.69, 313.29	96.12, 295.11	27.59	0.53	42.05	17.93	0.70
2005/01/20 06:42:10-06:43:30	818.51, 270.24	816.28, 238.58	27.32	1.11	6.96	5.58	0.56
2005/07/13 14:21:00-14:24:00	906.63, 184.05	905.22, 153.77	32.33	0.71	1.41	1.38	0.50
2005/07/30 06:30:30-06:33:30	-812.83, 132.40	-792.12, 114.50	35.18	0.30	17.78	14.65	0.55
2005/08/22 17:04:16-17:05:16	789.78,-252.62	812.71,-224.15	32.97	0.61	25.15	22.55	0.53
2005/09/10 21:32:00-21:34:00	-665.18,-248.19	-655.73,-268.29	16.31	1.12	9.33	4.90	0.66
2005/09/17 06:02:10-06:02:30	637.06,-270.29	600.36,-266.98	37.12	0.15	425.71	199.22	0.68

TABLE III

Pixon flare statistics

$Date/Time$	$centroid_1$	$centroid_2$	s	α	$Flux1$	$Flux2$	$\frac{Flux1}{Flux1+Flux2}$
2002/02/20 11:06:00-11:06:36	907.23, 249.43	902.63, 271.09	16.58	1.48	24.48	17.86	0.58
2002/07/23 00:41:00-00:44:40	-874.01,-242.75	-869.53,-216.92	32.39	0.74	3.53	3.59	0.50
2002/08/20 01:44:20-01:45:20	538.74,-270.07	524.75,-276.82	12.72	0.35	5.79	2.35	0.71
2002/09/08 01:42:20-01:43:20	-912.23,-198.62	-915.61,-175.86	17.48	1.47	28.32	10.58	0.73
2002/09/20 09:26:08-09:27:08	-832.81,-423.68	-838.82,-411.39	10.02	1.37	19.43	11.29	0.63
2002/11/09 13:21:04-13:22:04	419.37,-266.82	448.78,-251.76	25.00	0.44	36.34	16.43	0.69
2003/03/18 12:14:00-12:15:00	667.53,-159.92	697.22,-162.48	31.24	0.03	6.22	4.79	0.56
2003/06/02 00:13:28-00:14:28	931.17,-135.73	935.24,-120.19	19.07	0.66	13.33	7.83	0.63
2003/06/09 11:24:12-11:25:12	468.95, 228.76	476.47, 219.47	8.92	0.91	13.35	8.57	0.61
2003/06/10 11:06:16-11:07:16	650.23, 229.90	667.73, 218.86	18.51	0.47	10.11	4.04	0.71
2003/10/19 16:43:04-16:44:04	-814.85, 73.42	-796.93, 46.37	32.36	0.57	22.55	20.04	0.53
2003/10/24 02:48:26-02:50:52	-879.63,-329.56	-857.38,-345.78	45.21	0.19	17.93	14.31	0.56
2003/11/19 03:59:28-04:00:28	-96.05, -20.72	-88.34, -9.18	9.98	0.98	14.99	13.54	0.53
2004/10/30 16:23:48-16:24:48	429.37, 128.25	429.09, 152.39	17.63	1.47	88.18	43.46	0.67
2004/10/31 02:23:04-02:24:04	531.69, 162.01	520.46, 148.86	14.41	0.69	5.37	2.41	0.69
2004/10/31 05:31:20-05:32:20	543.33, 141.69	540.46, 160.35	13.67	1.54	16.26	12.24	0.57
2004/11/06 00:30:24-00:31:24	-74.72, 95.51	-89.32, 71.57	20.19	1.03	7.05	3.06	0.70
2004/12/01 07:09:56-07:11:56	-332.27, 106.29	-346.86, 149.88	33.97	1.18	7.97	2.18	0.79
2005/01/15 22:42:46-22:44:00	129.20, 312.26	95.31, 292.34	29.10	0.55	15.54	7.71	0.67
2005/01/20 06:42:10-06:43:30	818.25, 271.11	816.48, 238.63	27.67	1.14	7.36	6.42	0.53
2005/07/13 14:21:00-14:24:00	906.75, 183.23	904.54, 153.67	33.44	0.66	1.54	1.49	0.51
2005/07/30 06:30:30-06:33:30	-813.07, 132.22	-791.40, 116.76	35.46	0.25	18.18	12.36	0.60
2005/08/22 17:04:16-17:05:16	789.78,-252.62	812.92,-224.06	33.24	0.60	22.39	20.65	0.52
2005/09/10 21:32:00-21:34:00	-665.35,-248.22	-654.92,-268.84	17.02	1.08	9.12	4.58	0.67
2005/09/17 06:02:10-06:02:30	637.72,-270.74	601.56,-267.09	36.72	0.16	388.57	184.48	0.68

that there is a tight correlation between MEM NJIT, Clean, and Pixon fluxes. Figure 4b illustrates that MEM NJIT and Pixon are more similar to each other than either are to Clean.

The Clean fluxes in Figs. 4a and 4c seem to be systematically smaller than MEM or Pixon fluxes, particularly below 20 photons cm^{-2} s^{-1}. The difference is about a factor of 1.5 larger than the spread of the MEM-Pixon differences (RMS $\approx$ .05).

Fig. 4b shows two $\sim$5σ outliers for flare #19 that do not appear as outliers in Fig. 4a. They appear again as outliers in Fig. 4c. Since the mapping method common to Figs. 4b and 4c is Pixons, these components appear to have anomalously low fluxes in the Pixon method. This cannot be attributed to erroneous flux circles since the components are quite compact.

3.2. Centroids

We have computed the centroids of the weak and bright components for all the flares using each imaging method. We have shifted the MEM maps N and W by $\frac{1}{2}$ pixel ($1''$) to center the flux values in the pixels. The MEM-Clean centroid differences are shown in Fig. 5a. The differences are reasonably symmetric about the origin. The RMS spreads of the differences of the centroids are $1.32''$ for the brighter components and $1.95''$ for the fainter.

Fig. 5b shows the MEM-Pixon centroid differences. The centroids seem to be distributed symmetrically about the origin. The RMS differences are $1.15''$ and $1.94''$, similar to the MEM-Clean centroids.

Fig. 5c shows the Clean-Pixon centroid differences. There appears to be no significant shift of the centroids and the distributions are more compact: RMS = $0.87''$ and $1.23''$ for bright and faint components.

3.3. Histograms of Flux Asymmetry & Separation

We plot frequency histograms for the 25 flares of the flux asymmetry (F_R) in Fig. 6. The distributions are similar for the 3 methods, all of which indicate that F_R has a flat distribution up to $\sim$ 0.8. The cutoff at $\sim$ 0.8 is a selection effect, since we ignored single-component flares.

The de-projected separations of the components are plotted in Fig. 7. There seems to be a minimum between 20 and 25 Mm in all three histograms. This is probably the result

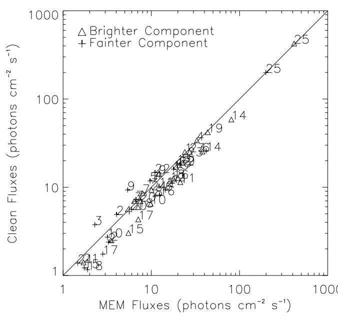

(a) MEM vs. Clean Fluxes For Bright and Weak Components

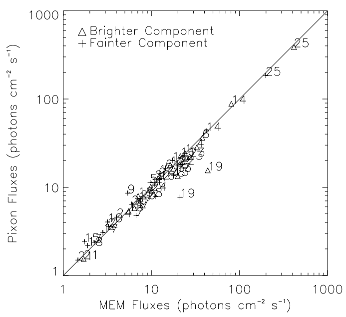

(b) MEM vs. Pixon Fluxes For Bright and Weak Components

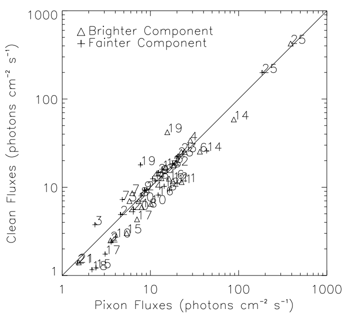

(c) Pixon vs. Clean Fluxes For Bright and Weak Components

Fig. 4.— (a) MEM NJIT fluxes vs. Clean fluxes for bright and weak components of all 25 flares. Notice that MEM NJIT fluxes have a tendency to be greater than their Clean counterparts, and there is a significant falloff for smaller Clean fluxes. The standard error of the difference of Clean flux from MEM flux is 0.07 in the log for the brighter component and 0.08 for the weaker components. (b) MEM NJIT fluxes vs. Pixon fluxes for bright and weak components of all 25 flares. The fluxes are well-correlated with only one pair of outliers. The standard deviation of the difference between log_{10} MEM and Pixon flux is 0.04 for the bright component and 0.06 for the weak component. (c) Pixon and Clean fluxes plotted against each other. Once again, there are more components that do not lie on the y=x line, suggesting that Clean maps provide poorer measures of source flux than MEM NJIT or Pixon. The standard deviation of log_{10} Pixon and Clean flux is 0.08 for the bright component and 0.10 for the weak component.

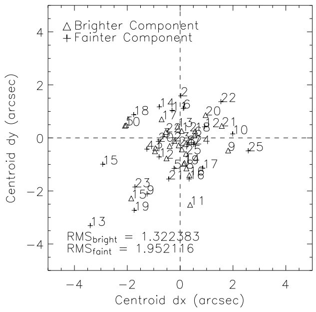

(a) Difference (MEM - Clean) in MEM and Clean Centroids

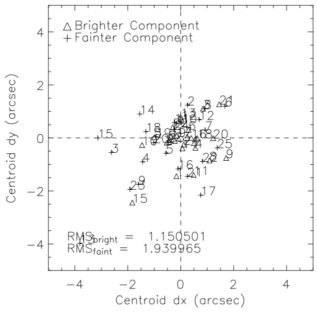

(b) Difference (MEM - Pixon) in MEM and Pixon Centroids

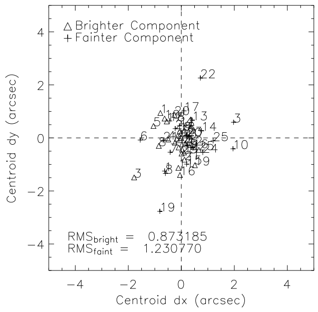

(c) Difference (Pixon - Clean) in Pixon and Clean Centroids

Fig. 5.— (a) The difference between centroids of the compact sources (Figs. 1-3) using MEM and Clean. The differences are reasonably symmetric about the origin, with RMS $= 1.32''$ for the bright components and $1.95''$ for the faint ones. (b) The difference between the centroids of sources using MEM and Pixons. The RMS values for bright and faint sources ($1.15''$ and $1.94''$) are similar to MEM-Clean differences. (c) The differences between centroids of the flare sources (Figs. 1-3) using Pixons and Clean. The distribution is centered close to the origin, with a smaller spread ($0.87''$ and $1.23''$ for bright and faint sources) than in the MEM-Clean and MEM-Pixon differences.

of small-number statistics, as the mean bin value is ~ 3, and the chance of having a value of 1 in a single bin is rather large.

3.4. Clean and MEM NJIT resolution compared

The following figures show that the MEM NJIT "super-resolution" (a term used by Cornwell & Evans, 1985) is about equivalent to using one additional (finer) RHESSI subcollimator. Figure 8 shows three double-component flares (rows 1, 2, and 3) mapped using the Clean algorithm with grids 2-8, 3-8, and 4-8 in columns 1, 2, and 3 (respectively). The instrumental resolutions of the 3 columns are, respectively, 4.3, 6.9, and $13''$.

Figure 9 shows the same flares (rows 1, 2, and 3) mapped using MEM NJIT with (u,v) circles 2-8, 3-8, and 4-8 in columns 1, 2, and 3 (respectively). When comparing the middle MEM NJIT map in the first row of Fig. 9 with the second Clean map in the first row of Fig. 8, the results are similar.

Comparison of the middle MEM maps with the column-1 Clean map again reveals similarities. The Clean maps show some low-level (10-20%) noise that is probably due to extended structure that is resolved out ("over resolved") by the finest subcollimator. MEM NJIT appears less susceptible to this effect.

Comparison of column-3 MEM maps with column-2 Clean maps does not show the same degree of similarity found above, but the Clean maps show some low-level noise. The column-3 MEM maps of the first two rows show only one component. Thus "super resolution" fails in these cases. The third flare mapped by MEM NJIT, however, shows two components much like the Clean map (column 2) with higher angular resolution.

We conclude that the MEM NJIT "super resolution" more clearly separates components that are not well separated by Clean. This result is similar to that found by Cornwell and Evans (1985) in which they compared VLA maps made using MEM in the C configuration with maps made in the B+C configuration with a factor of 3 higher resolution. In their case, MEM maps were more similar to the Clean maps with higher resolution uv-coverage, while in this case, the super-resolution of the MEM maps does not always agree with the Clean maps made with higher spatial resolution (one additional finer subcollimator).

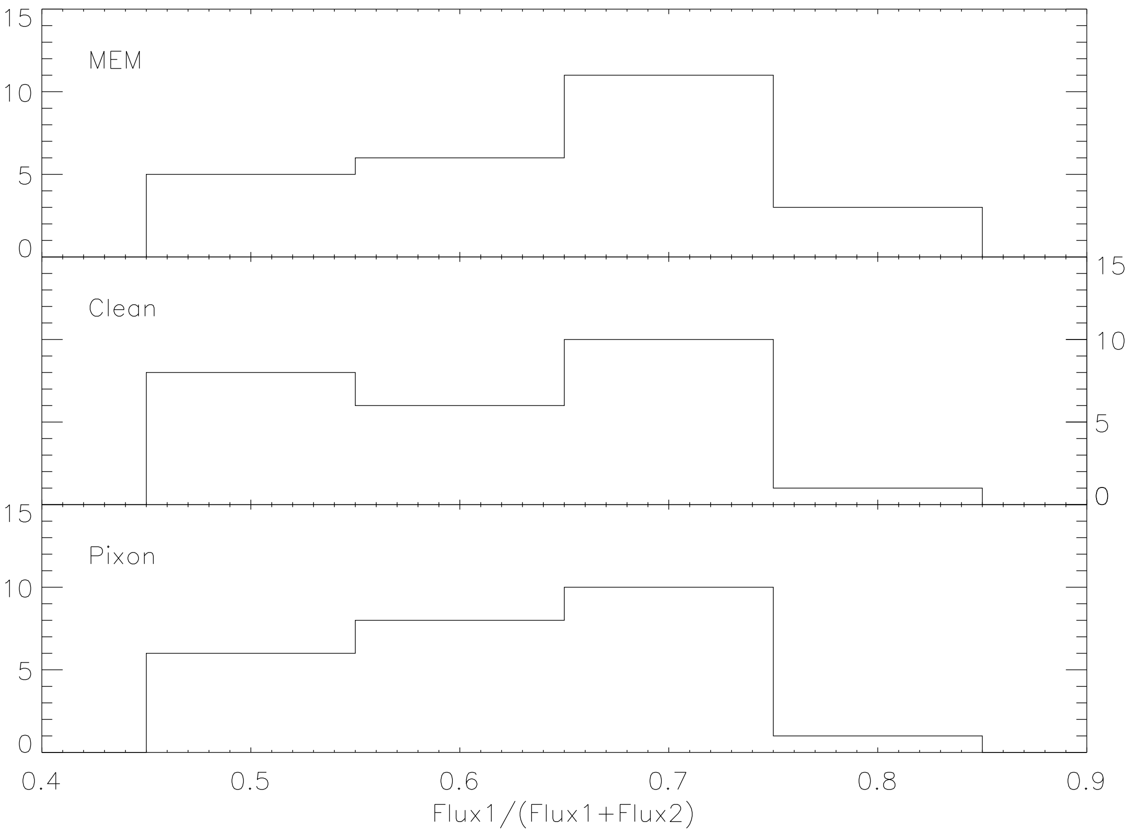

Fig. 6.— Histograms of the Flux Asymmetry ratio for MEM, Clean, and Pixons. The distributions are quite similar, showing approximately equal chances of a given asymmetry up to $F_R \sim 0.8$.

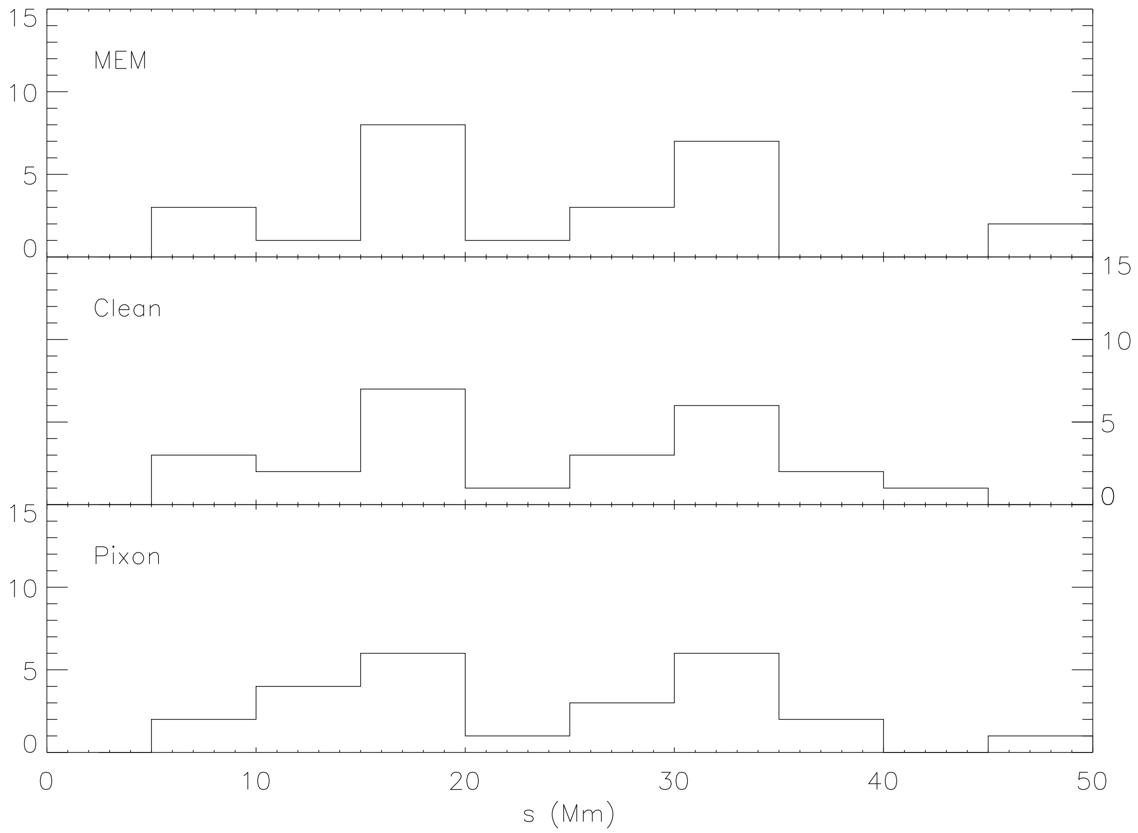

Fig. 7.— Histograms of the separations of the flare components in Mm for the 25 flares of Figs. 1-3 using MEM, Clean, and Pixons. The distributions appear to be double-bumped. See text for estimates of the statistical significance.

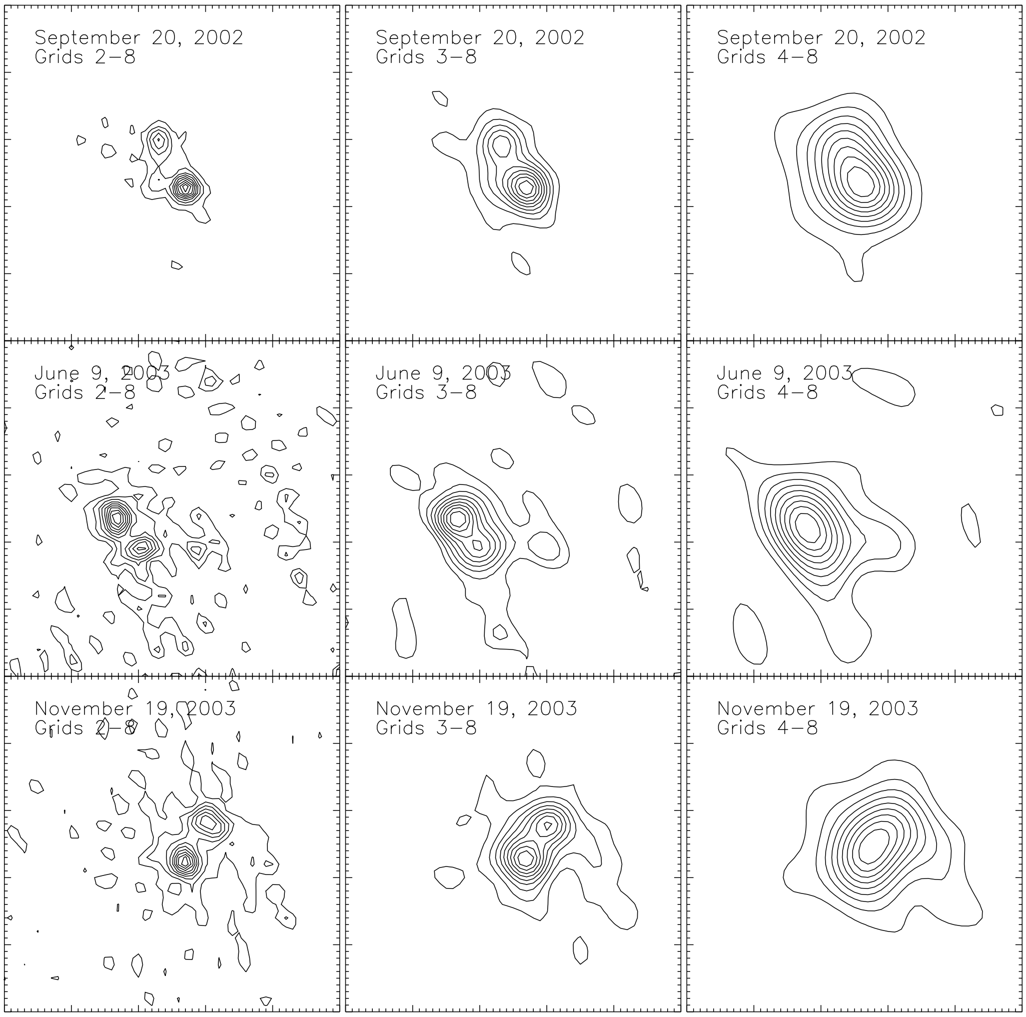

Fig. 8.— Clean maps of 3 flares with 3 different sets of subcollimators (Grids 2-8, 3-8, and 4-8). Contours start at 10% of the maximum, increasing at 10% increments to 100%.

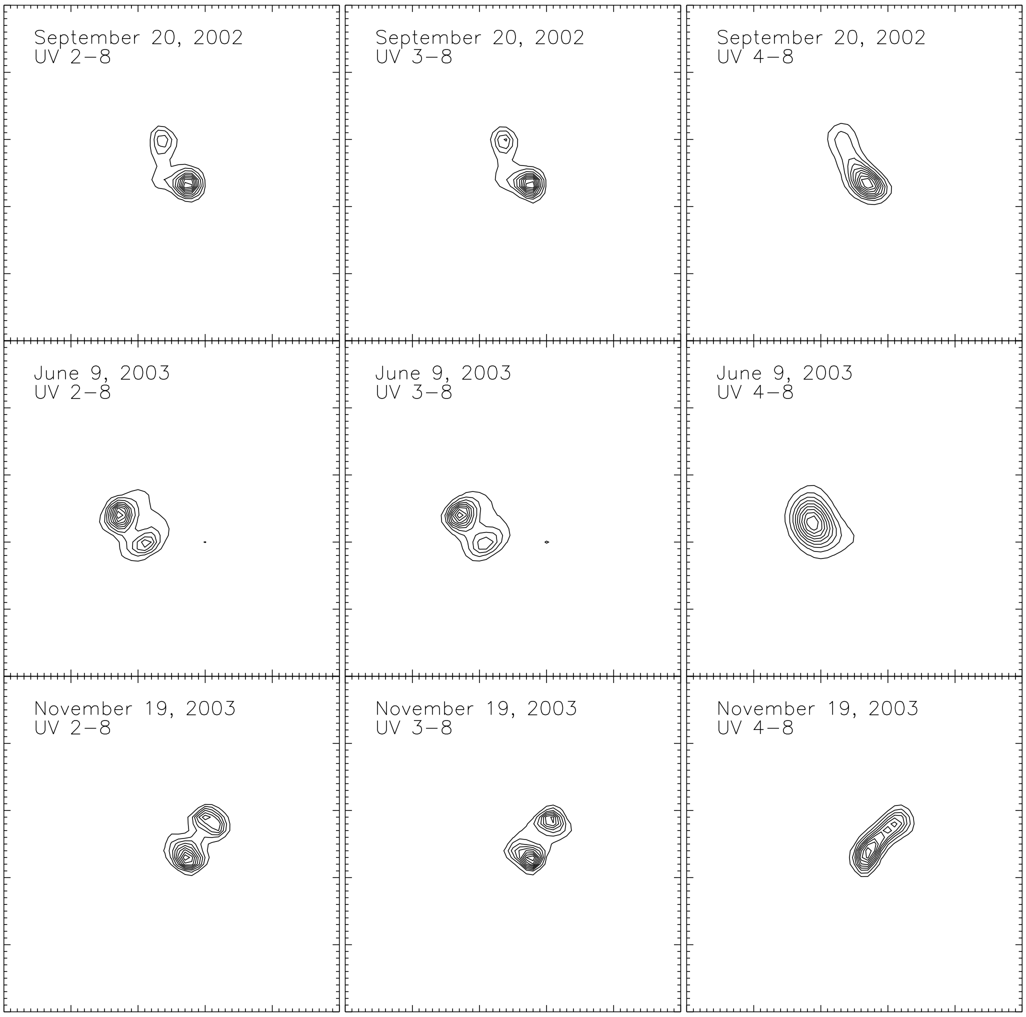

Fig. 9.— MEM NJIT maps of 3 flares with the equivalent (u,v) circle sets (UV 2-8, UV 3-8, and UV 4-8) and contours used in Clean.

3.5. Closing the Imaging Loop

We do a fundamental end-to-end test of MEM imaging to assess the "goodness-of-fit" of the maps to the original visibilities by comparing the visibilities constructed from MEM maps with the original visibilities. We compute the visibilities derived from the MEM maps themselves. This is simply a pixel-by-pixel sum of the quantities V_j (equation 1) for all of the u and v values used in the mapping. In Fig. 10 we show plots of the amplitude vs. roll angle for 5 UV circles for two flares (# 2 and 18). Solid lines are for the original visibilities and dashed lines are for model visibilities computed from the maps. The normalized χ^2 statistics for these curves are shown in Fig. 10 for each flare and uv circle.

Fig. 11 shows plots of the original visibility phase profiles (crosses) and the model phase profiles (triangles) computed from the MEM NJIT maps. There appears to be a roll-angle shift of about one roll bin between the phase profiles, most evident at the finer spatial scales (uv circles 4 and 5). The cause of this roll shift is unknown. Error bars have been constructed from the amplitude error bars by assuming that the real and imaginary parts of the visibilities are equal.

4. Conclusions

We have developed and validated a new Maximum Entropy Method (MEM NJIT) based on visibilities for RHESSI hard X-ray imaging. In several ways this new MEM utility is superior to the current mapping algorithms in the RHESSI software. The maps produced with MEM NJIT appear qualitatively and quantitatively similar to the RHESSI Pixon maps, and share Pixon's flux reliability, low sidelobes, and flat background. However, MEM NJIT is two orders of magnitude faster in execution. The program also executes more rapidly than Clean, and the flare components in maps display less source confusion than Clean.

On the negative side, however, we find that there is somewhat larger scatter ($\sim 0.5''$) in the calculation of centroids of components in our MEM NJIT maps. It is possible that this is caused by the incomplete sampling in the RHESSI visibilities or by nonlinear effects in the MEM NJIT algorithm. Another failure of the algorithm is that the "super-resolution", common also to Pixons, does not appear to be a reliable indicator of sizes. This is demonstrated by test images using Clean with different upper cutoffs for spatial scales.

Our "end-to-end" tests of MEM NJIT show that the visibility amplitudes and phases constructed from the MEM maps agree with the original RHESSI visibilities. Agreement between the profiles (Fig. 10) of the original and model amplitude curves seems to improve with decreasing spatial scale. This is borne out by the χ^2 values shown for each profile in

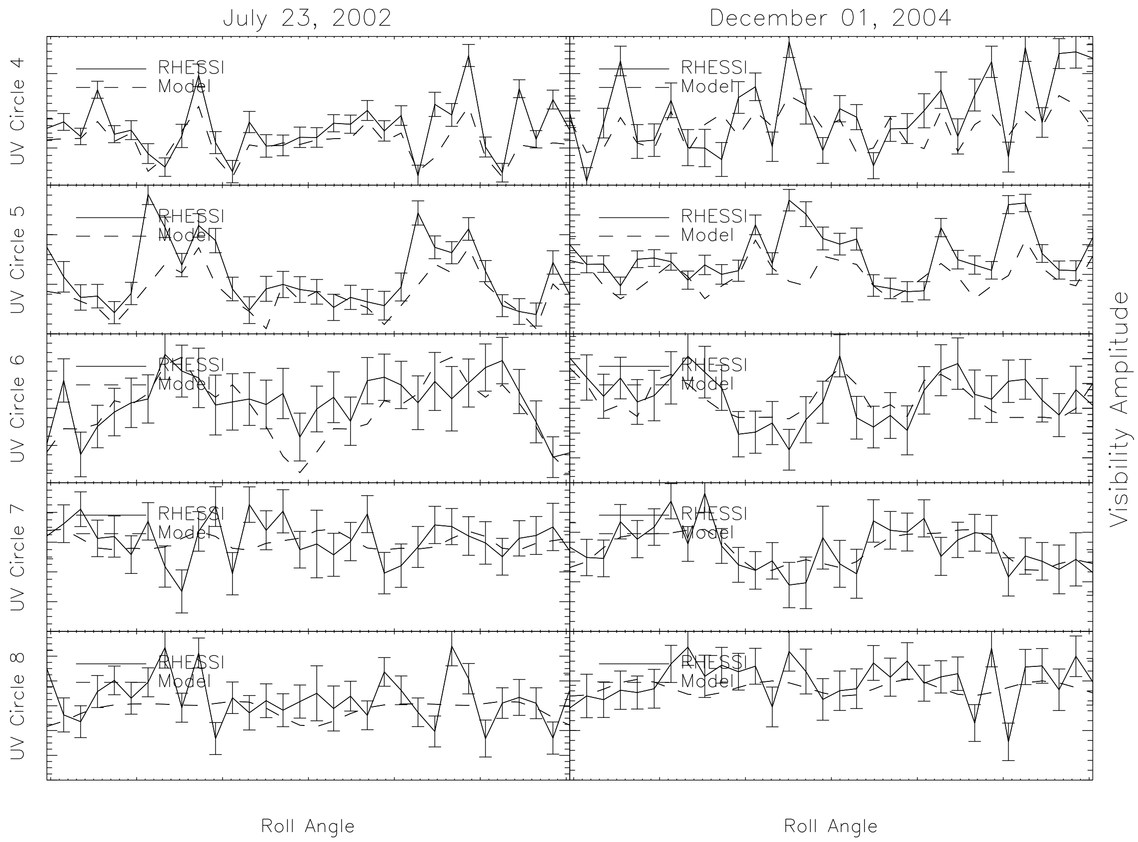

Fig. 10.— Plots of the original visibility amplitudes (solid curves) and model amplitudes (dashed curves) computed from MEM NJIT maps. The errorbars are 1-sigma uncertainties obtained from the software that converts RHESSI modulation into visibilities. Agreement between the curves seems to improve with decreasing spatial scale. The χ^2 statistic is shown for each profile in the lower right hand corner.

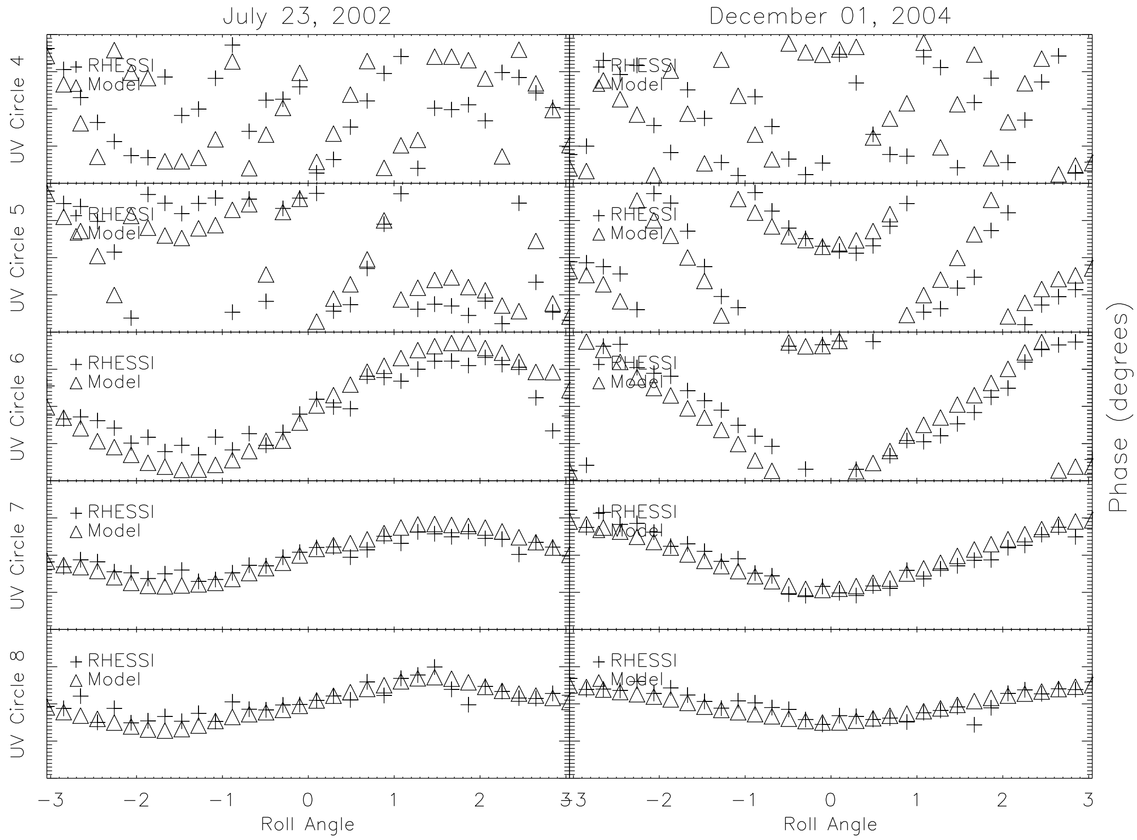

Fig. 11.— Plots of the original visibility phase profiles (crosses) and the model phase profiles (triangles) computed from the MEM NJIT maps. There is an apparent roll-angle shift between profiles, most evident at the finer spatial scales (uv circles 4 and 5). The χ^2 statistic is shown for each profile in the lower right hand corner.

the bottom right corners of the plots.

5. Acknowledgements

The research of E.J.S. was supported by RHESSI grants from NASA/GSFC to the University of Maryland. R.L.P. was supported by an internship grant from the RHESSI team and the Catholic University of America in the Summer of 2005, and a Research Assistantship from CUA afterwards.

6. References